Article

Fractal Characterization of Particle Size and Coordinate Distribution of Dispersed Phase in the Steelmaking Process of Combined Blowing Conversion

Shiyi Chen [1], Xiaolei Zhou [1], Zhihao Zheng [2], Ren Chen [3,*], Shan Yu [3] and Chunyang Shi [3]

[1] School of Metallurgy and Energy, Kunming University of Science and Technology, Kunming 650093, China; sheachen@163.com (S.C.); zhouxiaolei81@163.com (X.Z.)

[2] School of Metallurgy, Northeastern University, Shenyang 110819, China; haohao2020@yeah.net

[3] School of Metallurgy and Materials Engineering, Liaoning Institute of Science and Technology, Benxi 117004, China; windhat@163.com (S.Y.); scy9090@126.com (C.S.)

* Correspondence: toughold@163.com

Abstract: A two-dimensional water model was used to simulate the process of combined blowing. The effect of boundary conditions on the size and coordinate distribution of the dispersed phase was investigated. The results showed that the frequency of the dispersed phase at a certain size level is proportional to its size; the coordinates of the dispersed phase can be expressed in a dimensionless form that shows its uniformity of distribution. An empirical equation for the influence of the boundary conditions on the size and coordinate distribution of the dispersed phase in combined blowing process is also presented.

Keywords: combined blowing converter; water model; dispersed phase; particle size distribution; coordinate distribution; fractal characterization

1. Introduction

In most metallurgical reaction systems, the overall rate of the reaction between the dispersed phase and the continuous phase is determined by a number of physical processes, such as diffusion conditions and dispersion (emulsification) conditions [1]. For converter blowing and other types of metallurgical reactors, accelerating the exchange of substances often determines the efficiency of the processes. Therefore, generating droplets of exchanged substances has become one of the key research topics in related fields. When the mass transfer between the droplets and the melt dominates the material exchange process, it is important to determine its mass transfer coefficient under various boundary conditions [2]. If an accurate mass transfer coefficient is obtained, it is possible to calculate the amount of substance exchange for reactions such as dephosphorisation and desulfurization after determining the interfacial area and knowing the equilibrium constants [3]. In current production practice and experimental research, the mass transfer coefficient is generally unknown due to the complexity of the system, and the reaction rate of the substances concerned can only be estimated within a certain period of time. Apparently, this method contains a certain degree of hysteresis, and the estimation of the interfacial area of the reaction contains a certain degree of uncertainty. Therefore, most of the metallurgical simulation of the mass transfer coefficient is generally reduced to the determination of the reaction equilibrium constants. The determination of the coefficient is generally reduced to the determination and calculation of the volumetric mass transfer coefficient. Under certain external boundary conditions, the mass transfer coefficient should be a certain value; thus, in order to determine the mass transfer coefficient, the interfacial area has to be calculated accurately and quantitatively.

The size of the slag–metal interfacial area in the process of combined blowing conversion is related to the amount of dispersed phase and the particle size distribution of

the dispersed phase. In addition, it is also related to the coordinate distribution of the dispersed phase since the coordinate distribution determines the residence time of the dispersed phase in the continuous phase and thus the interfacial area per unit of time [4]. The resolution of the number of dispersed phases, the size class distribution, and the coordinate distribution currently mainly rely on statistical theoretical approaches, and as a result of their influence, the isoconcentration curves or surfaces of the dispersed phases, whether obtained by numerical simulations or achieved experimentally, are almost depicted as continuous smooth curves or surfaces with a theoretical basis that is entirely based on Euclid geometry [5]. However, just as the lines, surfaces and bodies in nature are not always smooth [6]. In metallurgical reaction processes such as converter blowing, the slag–metal dispersed phase interfaces are often rough and broken due to turbulence, and the boundaries may be discontinuous or continuous but not differentiable, which are mathematically called "pathological curves or surfaces" [7]. Fractal geometry, as proposed by Mandelbrot, is used to describe these geometrical objects with highly irregular or fragmented geometry objects [8]. The main purpose of this study is to analyze the particle size and coordinate distribution of the slag and metal dispersed phases in the continuous phase during the smelting process of combined blowing conversion with the help of fractal theory and then provide a quantitative calculation method for obtaining the area of the slag–metal reaction interface.

2. Experimental Equipment and Analysis Methods

2.1. Experimental Equipment

A Plexiglass model was used to simulate the longitudinal section of an industrial combined blowing convertor, and the experimental setup is shown in Figure 1. Metal and slag were simulated by using water oil; a digital camera was used for image acquisition (resolution of 0.277×0.277 mm^2/pixel), and the two-dimensional images were processed by a computer to extract the dispersed phase image data. The experimental parameters are listed in Table 1.
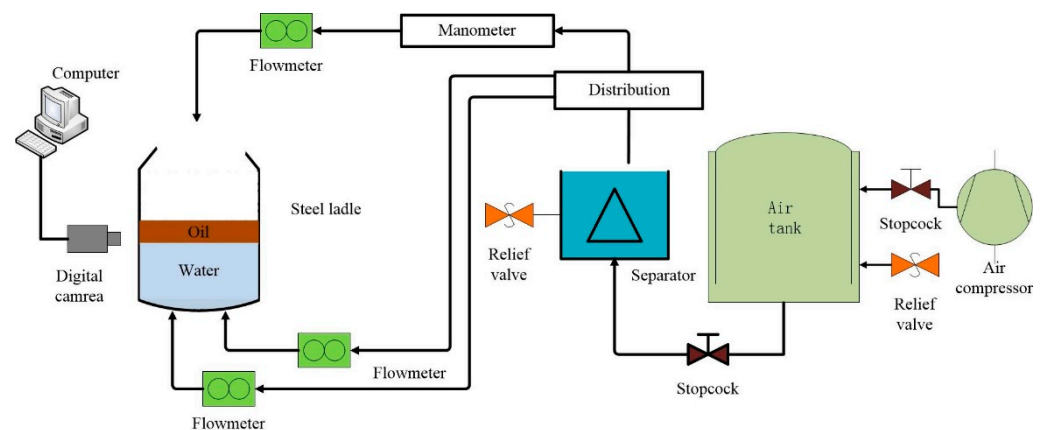

Figure 1. Experimental apparatus.

The geometric similarity between the model and the prototype was guaranteed in the experiments, and the geometric similarity ratio was deemed to be 1:6. The top blowing gas flow rate and bottom blowing gas flow rate were determined according to the Buckingham Π Theorem [9]. Furthermore, in order to ensure the similarity of dynamics between the model and the prototype, it is crucial to ensure that the *Froude* number Fr_m of the model is equal to the *Froude* number Fr_m' of the prototype, which can be written as follows:

$$\frac{\rho_a V_M^2}{\rho_w g d_M} = \frac{\rho_{O_2} V_{O_2}^2}{\rho_m g d_I} \tag{1}$$

$$\frac{V_M}{V_{O_2}} = (\frac{\rho_{O_2}\rho_w}{\rho_a\rho_m})^{0.5}(\frac{d_M}{d_I})^{0.5} \tag{2}$$

$$Q_a = V_M(\frac{\pi}{4}ed_M^2) \times 3600 \tag{3}$$

$$Q_{O_2} = V_{O_2}(\frac{\pi}{4}ed_I{}^2) \times 3600 \tag{4}$$

$$\frac{Q_a}{Q_{O_2}} = (\frac{V_M}{V_{O_2}})(\frac{d_M}{d_I})^2 = 0.004678 \tag{5}$$

To calculate the bottom blowing gas flowrate, the Froude number of the model Fr_m must be equal to the Froude number of the prototype Fr_m.

$$\frac{\rho_a V_M^2}{\rho_w g d'_M} = \frac{\rho_{N_2} V_{N_2}^2}{\rho_m g d'_I} \tag{6}$$

$$\frac{V'_M}{V_{N_2}} = (\frac{\rho_{N_2}\rho_w}{\rho_a\rho_m})^{0.5}(\frac{d'_M}{d'_I})^{0.5} = 0.386\left(\frac{d'_M}{d'_I}\right)^{0.5} \tag{7}$$

$$Q'_a = V'_M(\frac{\pi}{4}n_1 d'_M{}^2) \times 3600 \tag{8}$$

$$Q_{N_2} = V'_{N_2}(\frac{\pi}{4}n_2 d'_I{}^2) \times 3600 \tag{9}$$

$$\frac{Q'_a}{Q_{N_2}} = 0.386(\frac{d'_M}{d'_I})^{0.5}(\frac{n_1}{n_2})(\frac{d'_M}{d'_I})^2 = 0.00146 \tag{10}$$

Table 1. Main parameters of the experiment.

Parameter		Converter	Water Model
Height	(mm)	4800	800
Diameter (width)	(mm)	3000	500
Thickness	(mm)	-	50
Bath depth	(mm)	708	118
Blowing mode		Combine-blowing	Combine-blowing
Blowing gas	(Nm^3/h)	Tonnage oxygen	Air
Bottom gas	(Nm^3/h)	Nitrogen	Air
The Density of molten	(kg/m^3)	7000	1000
The Density of slag	(kg/m^3)	3200	808
Diameter of the throat	(mm)	38	6.3
Angle of the throat		12	12
Number of the throat		4	4
Throat circle diameter	(mm)	140	23.3

2.2. Experimental Method of Image Processing

The experimental digital image consists of two types of regions with many different grayscales. The grayscale histogram of the image has a distinct bimodal form, corresponding to the grayscale ranges of two regions. These two peaks can be separated by choosing an appropriate threshold.

The optimal threshold of the image is determined by using the minimum error method [10–16]. Due to the fact that the digital images of dispersed phase contain two types of brightness regions—continuous phase (background) and dispersed phase (object)—their grayscale histograms can be represented by the brightness density functions $p_1(x)$ and $p_2(x)$, which are the sum or weighted sum of two unimodal density functions (one

corresponds to the bright region and the other one peak corresponds to the dark region). If $p_1(x)$ and $p_2(x)$ are normal density functions, the mixed brightness density function is given by the following:

$$p(x) = P_1 p_1(x) + P_2 p_2(x) = \frac{P_1}{\sqrt{2\pi}\beta_1} \exp \frac{-(x-\mu_1)^2}{2\beta_1^2} + \frac{P_2}{\sqrt{2\pi}\beta_2} \exp \frac{-(x-\mu_2)^2}{2\beta_2^2} \quad (11)$$

where μ_1 and μ_2 are the average brightness of the two regions, β_1 and β_2 are the standard deviation of brightness in the corresponding area, and P_1 and P_2 represent the prior probability of background and object appearance, respectively.

Since $P_1 + P_2 = 1$ as the constraint condition must be satisfied, the mixed density function $p(x)$ is a function of five unknown parameters. After obtaining these parameters, the optimal threshold can be determined.

In this case, with T as the threshold, pixels with grayscale levels lower than T are considered as continuous phase (background), while pixels greater than T are considered as dispersed phase (object) [17]. Therefore, the probability of misclassifying points on the object to points on the background is

$$E_1(T) = \int_{-\infty}^{T} p_2(x)dx \quad (12)$$

Similarly, the probability of misclassifying points on the background to object points is

$$E_2(T) = \int_{T}^{\infty} p_1(x)dx \quad (13)$$

Therefore, the total error probability is

$$E(T) = P_2 E_1(T) + P_1 E_2(T) \quad (14)$$

In order to determine the threshold value with the smallest error of classification, the derivative of E(T) over T is deduced and defined as 0; then,

$$P_1 p_1(T) = P_2 p_2(T) \quad (15)$$

Substitute the normal density function into the above equation and followed this by taking the logarithmic form and simplifying it to obtain a quadratic equation:

$$\begin{aligned} AT^2 + BT + C &= 0 \\ A &= \beta_1^2 - \beta_2^2 \\ B &= 2\left(\mu_1\beta_2^2 - \mu_2\beta_1^2\right) \\ C &= \beta_1^2\mu_2^2 - \beta_2^2\mu_1^2 + 2\beta_1^2\beta_2^2 \ln(\beta_2 P_1/\beta_1 P_2) \end{aligned} \quad (16)$$

At this point, the optimal threshold is the average of the two means.

$$T = \frac{\mu_1 + \mu_2}{2} + \frac{\beta^2}{\mu_1 - \mu_2} \ln(P_2/P_1) \quad (17)$$

If the grayscale ranges of the dispersed and continuous phases partially overlap, two values of T_1 and T_2 (assuming $T_1 > T_2$ and the overlapping region of grayscale is in between T_1 and T_2) are used for thresholding:

$$g(x,y) = \begin{cases} 1 & f(x,y) \geq T_1 \\ 0 & f(x,y) \leq T_2 \end{cases} \quad (18)$$

In a scenario where $T_2 < f(x,y) < T_1$, the affiliation of the pixel can be determined by checking the affiliations of the majority pixels within the zone under consideration.

Alternatively, it is considered that the pixel and the adjacent one belong to the same category based on the difference in the grayscale levels of the two pixels.

According to Equation (18), a 256-level grayscale bitmap can be converted into a monochrome black and white bitmap. The original image and dispersed phase extraction results of the experiment are shown in Figure 2.
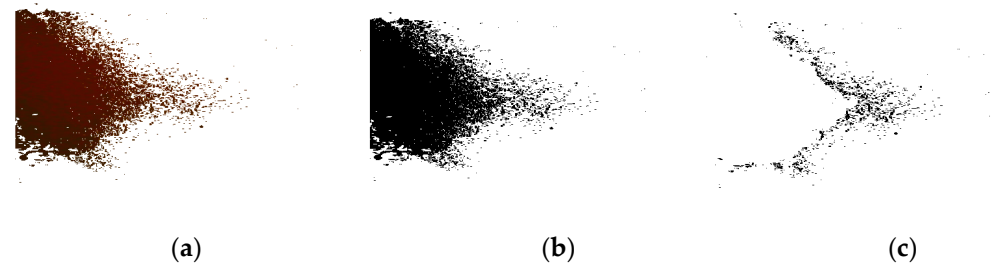

(a)	(b)	(c)

Figure 2. Original digital photos and results of image processing. (**a**) Original digital photos; (**b**) black and white bitmap; (**c**) dispersed phase bitmap.

2.3. Methods for Studying Particle Size Distribution in Dispersed Phase

The experimentally obtained image can be considered as a cross-section in three dimensions. The dispersed phase can be considered as a set of clusters in a two-dimensional pixel space. The distribution of the clusters can be described by a proportional function since a particular physical property within the system varies proportionally [18–21]. Table 2 lists the statistical results of the dispersive phase under a certain boundary condition.

Table 2. Number and dimension of the dispersed phase.

s (pixel)	n	N	s (pixel)	n	N
1	85	196	11	1	10
2	27	111	12	1	9
3	34	84	13	2	8
4	13	50	14	1	6
5	7	37	16	1	5
6	6	30	17	1	4
7	4	24	25	1	3
8	4	20	27	1	2
9	3	16	35	1	1
10	3	13			

The relationship between the size of the dispersed phase and its frequency of occurrence is expressed in logarithmic coordinates, and the linear relationship shows that the frequency of occurrence of a dispersed phase with a certain size is proportional to its size [22–24]. Mathematically, this relationship can be expressed as follows:

$$N = S^M \tag{19}$$

where N is the number of clusters with a size greater than or equal to S, and M is the slope. The distribution of the dispersed phases at each size level can be determined by M under the condition. As shown in Figure 3, ln(N) and ln(S) are linearly related, and $|M|$ reflects the particle size distribution under this boundary condition, with a larger $|M|$ indicating a larger proportion of dispersed phases with a smaller size.
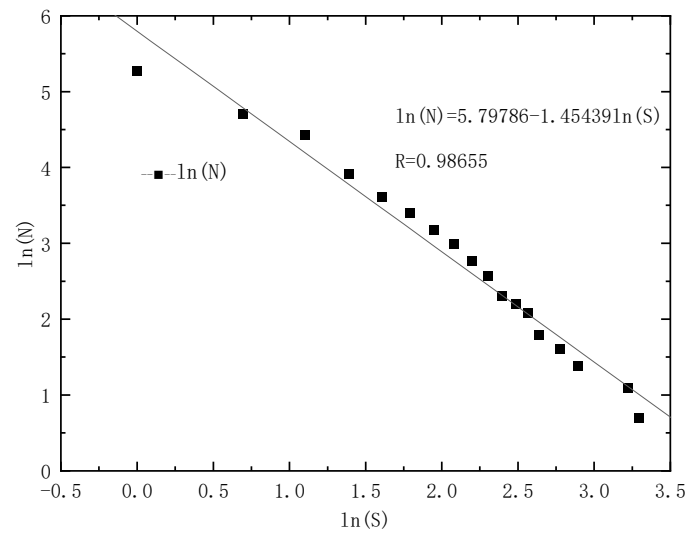
Figure 3. Logarithmic relationship between S and N.

2.4. Methodology for Analyzing Dispersed Phase Coordinate Distributions

Taking the intersection of the upper edge of the oil layer and the center line of the flowing strand as the coordinate origin (the *x*-axis along the horizontal direction) and the center line of the flowing strand as the *y*-axis, the extracted scattered phase images are processed, and the scattered phases larger than one pixel can be regarded as mass points and averaged according to the following equation.

$$\left(x = \sum_{i=1}^{n} x_i/n, y = \sum_{i=1}^{n} y_i/n\right) \tag{20}$$

where n is the number of pixels in the dispersed phase, and (x_i, y_i) is the coordinates of the pixels in the dispersed phase.

Since the number of dispersed phases and their coordinates vary greatly depending on the boundary conditions, the coordinates must be dimensionless, and the definition can be written as follows.

$$\left(x'_m = (x_m - r)/(R - r), y'_m = y_m/\delta\right) \tag{21}$$

where x'_m and y'_m are the dimensionless horizontal and vertical coordinates of the metal droplet, r is the impact pit radius, R is the model radius, and δ is the slag layer thickness, respectively.

In the equation above, the droplet dispersion phase horizontal x_s and vertical coordinates y_s are also dimensionless.

$$\left(x'_s = (x_s - r)/(R - r), y'_s = y_s/h\right) \tag{22}$$

where x'_s and y'_s are the dimensionless horizontal and vertical coordinates of the slag droplet, respectively. h is the depth of the molten bath. Table 3 shows the statistical results of the dispersed phase transverse coordinates under certain boundary conditions, and Figure 4 depicts the dimensionless distribution of the dispersed phase.

In Figure 4, L represents the range of dimensionless transverse coordinates of the dispersed phase, P denotes the percentage of the number greater than or equal to this range, and K represents is the mean of the rate of change in the inverted S-shaped regression curve.

$$K = \left(\int_0^1 P'\,dL\right)/(1 - 0) \tag{23}$$

A larger $|K|$ value leads to an increase in the proportion of dispersed phase that is close to the origin, thus giving rise to a more concentrated distribution of the dispersed phase. Conversely, a smaller value corresponds to a more uniform distribution. For the dimensionless longitudinal distribution analysis, the method is slightly different from the transverse analysis, i.e., a larger value of $|K|$ indicates a larger proportion of dispersed phase that is close to the upper edge of the slag layer. Thus, the value of K can be used to indirectly describe the regularity of the dispersed phase coordinate distribution.

Table 3. Distribution statistics of the dispersed phase.

F	n	DL_r	P
$0 < x_m' \leq 0.1$	18	0.02894	1
$0.1 < x_m' \leq 0.2$	98	0.15755	0.9711
$0.2 < x_m' \leq 0.3$	118	0.18971	0.8135
$0.3 < x_m' \leq 0.4$	104	0.16720	0.6238
$0.4 < x_m' \leq 0.5$	72	0.11576	0.4566
$0.5 < x_m' \leq 0.6$	78	0.12540	0.3408
$0.6 < x_m' \leq 0.7$	105	0.16881	0.2154
$0.7 < x_m' \leq 0.8$	15	0.02412	0.0466
$0.8 < x_m' \leq 0.9$	3	0.00482	0.0225
$0.9 < x_m' \leq 1.0$	11	0.01768	0.0177

$$P = A_2 + (A_1 - A_2)/(1 + \exp((L-L_0)/dL))$$
$$R^2 = 0.99457$$
$$A_1 = 1.15763$$
$$A_2 = -0.05029$$
$$L_0 = 0.45475$$
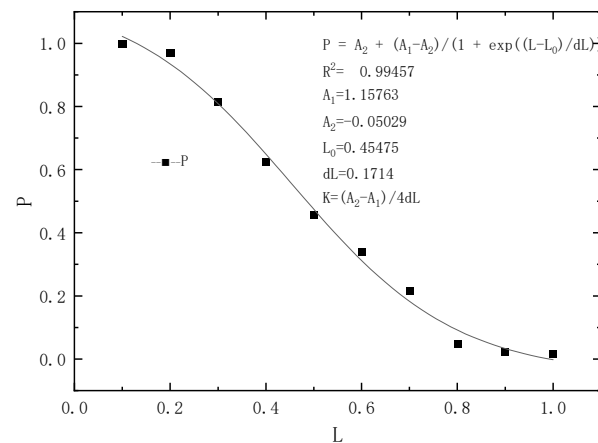$$dL = 0.1714$$
$$K = (A_2 - A_1)/4dL$$

Figure 4. Dimensionless distribution of the dispersed phase.

3. Results and Discussion

3.1. Particle Size Distribution of the Dispersed Phase of Metal Droplets

Figure 5a,b show the metal droplet size distribution $|M_m|$ versus the boundary conditions. As shown in the figure, $|M_m|$ increases with decreasing H and increasing Q_T, while at a shallow impact depth with a high H or low Q_T, $|M_m|$ increases with increasing Q_B. When H is decreased by 50% and Q_T is increased by a factor of two, $|M_m|$ will increase by a factor of two. At low H and large Q_T, there is a peak value of $|M_m| = 3.1$ with Q_B. According to the droplet critical diameter relation [25] $/d_T = [6\sigma\cos\alpha/g(\rho_m - \rho_s)]0.5$, as the impact pit depth h increases, α decreases, and then d_T decreases. At this time, the interfacial flow velocity u_i is much larger than the critical flow velocity $u_{i, crit}$, and the diameter of the droplets rapidly decreases when they leave the parent phase. Thus, the metal droplets are emulsified into the slag with a high proportion of small scale. As H decreases (H $\leq$ 110 mm) and Q_T ($Q_T \geq 35$ Nm^3/h) increases, vertical and horizontal oscillations occur in the impact pit, while the intervention of bottom blowing ($Q_B \geq 0.8$ Nm^3/h) intensifies the amplitude of the above oscillations, thus increasing α instead, and d_T becomes larger. It can be considered that when the top and bottom blowing is small, their interaction is weak, and their respective independent formation of vortex is driven by the liquid bath movement, giving rise to a negligible interference. While the top and bottom

blowing intensity are very large, the top and bottom blowing formation of vortex cross, and the mutual influence of the two cannot be ignored. In addition, with the increase in S/M, it is more difficult to form the 'effective impact area' than in a scenario with a low metal/slag ratio. Therefore, the effect of external gas supply on the change of $|M_m|$ is relatively delayed in the high metal/slag ratio condition, and it can be assumed that under the low metal/slag ratio condition, $|M_m|$ is more sensitive to the change of the external boundary conditions (the lance height H, the top-bottom combined blowing flow rate Q_B) than the high metal/slag ratio condition.

(**a**)   (**b**)
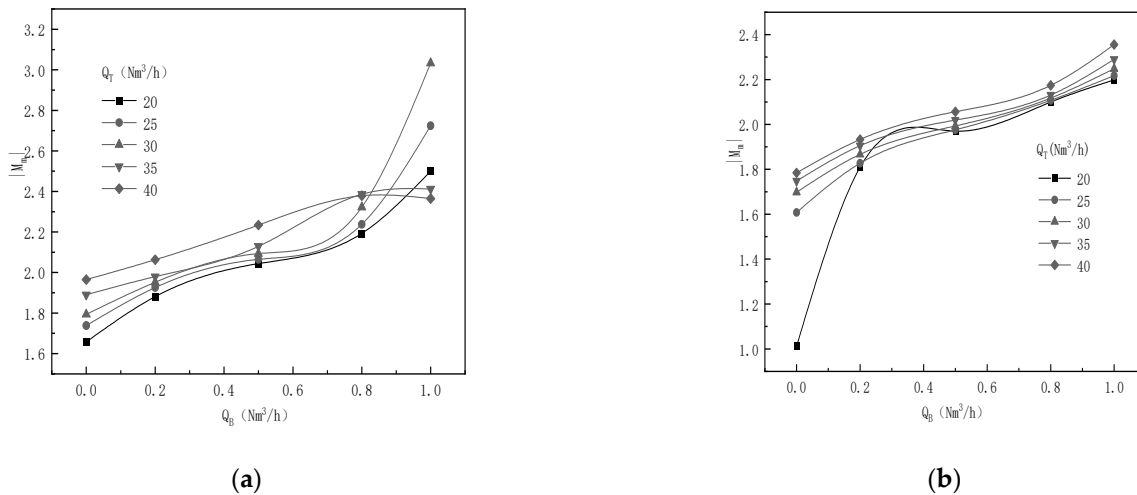
Figure 5. Relationship between $|M_m|$ and bottom blowing under various lance positions with different S/M ratios: (**a**) S/M = 14/118, H = 80 mm; (**b**) S/M = 45/118, H = 170 mm.

3.2. Particle Size Distribution of the Dispersed Phase of Slag Droplets

Figure 6a,b show the relationship between the droplet size distribution $|M_s|$ and the boundary conditions As can be seen, Q_T has a negligible effect on $|M_s|$ when H is high ($\geq$150 mm) or S/M is large ($\geq$37/118), and its variation is mainly influenced by Q_B; thus, it can be assumed that top blowing only plays a role in the variation of $|M_s|$ under low H or small S/M conditions. An increase in Q_B increases cosα, decreases d_T, and increases $|M_s|$. Unlike the extreme value of $|M_m|$, there is no such trend in the variation of $|M_s|$, which is mainly due to the difference in the formation and dispersion mechanisms of metal and slag droplets. The metal droplets are no longer subject to the forces of the liquid bath after leaving the parent phase; the particle size does not change, and after falling back into the slag phase, the slag layer is dominated by laminar flow, so the chance of continuing to split into smaller droplets becomes wea. The droplets, once generated, remain in the liquid bath and are subject to various forces, which may be both longitudinal and transverse tensile stresses and shear stresses. Therefore, it is more likely to be further split into smaller droplets, resulting in a large $|M_s|$ value.

It should be noted that the above analysis only discusses the relationship between the particle size distribution of the dispersed phase and its scale under various boundary conditions in the combined blowing conditions without involving the size of the specific scale value and the total amount of the dispersed phase, so it can only be used as a kind of possibility analysis of the size of the interfacial area between the metal and slag and cannot be used for the calculation of the interfacial size.
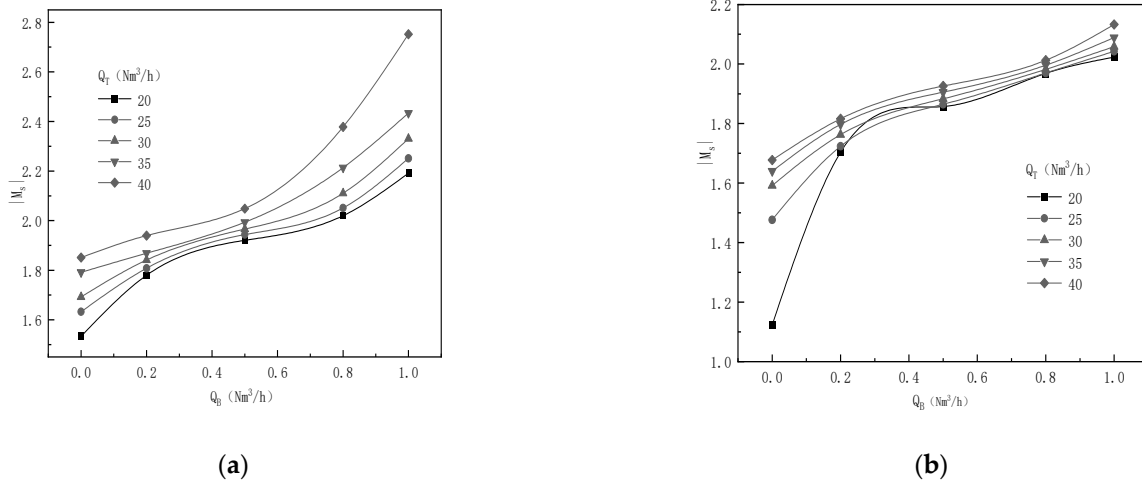
Figure 6. Relationship between $|M_s|$ and bottom blowing under various lance positions with different S/M ratios: (**a**) S/M = 14/118, H = 80 mm; (**b**) S/M = 45/118, H = 170 mm.

In addition, the different $|M|$ values obtained under various experimental boundary conditions can thus be related to the calculation of the interfacial area of emulsified metal and slag. However, this calculation is only limited to two-dimensional cases. Therefore, if the three-dimensional interfacial area is required, the Law of Additive Codimensions in the fractal theory must be applied to convert the two-dimensional cross-section codimensions under experimental conditions into the surface codimensions of a three-dimensional image, so that quantitative calculations of metal–slag interfacial area can be realized.

3.3. Dimensionless Coordinate Distribution of the Dispersed Phase of Metal and Slag Droplets

Figure 7a,b show the metal drop horizontal and vertical coordinate distributions $|K_{mx}|$, $|K_{my}|$ versus the boundary conditions. As can be seen, with the increase in H, both hand u_i decrease, so the horizontal component of u_i decreases and falls into the slag phase mainly near the origin, and $|K_{mx}|$ increases($|K_{mx}|$ can be up to 0.98). An increase in Q_T increases h, and although u_i increases, the angle between u_i and the horizontal direction also increases, and the effect of the angle on the fractional velocity may be greater, and the horizontal fractional velocity of the metal droplets decreases.
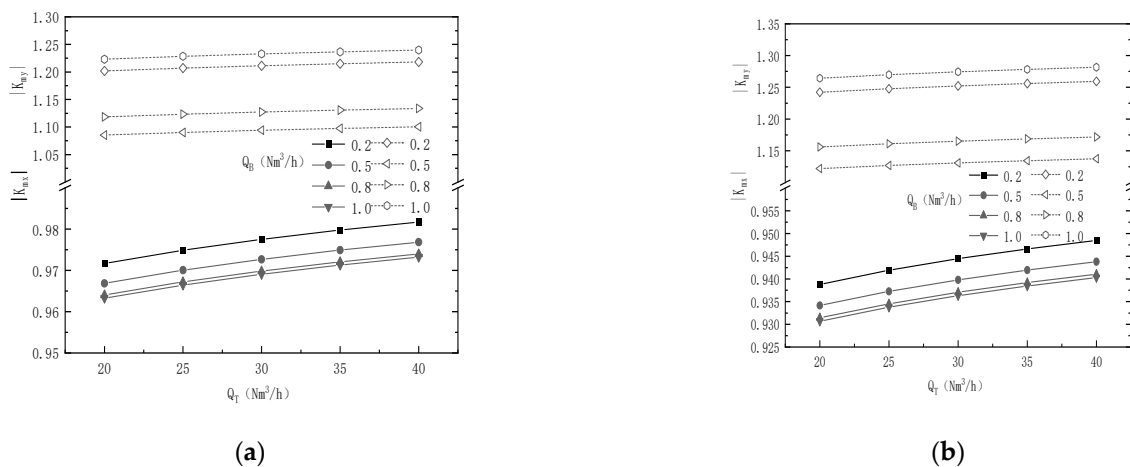

Figure 7. Relationship between $|K_m|$ and top blowing under various lance positions with different S/M ratios: (**a**) S/M = 45/118, H = 170 mm; (**b**) S/M = 14/118, H = 80 mm.

Therefore, an increase in Q_T causes the metal droplets to be unevenly distributed along the x-direction. As S/M increases, the horizontal fractional velocity at the detachment

point decreases and $|K_{mx}|$ increases (when S/M increases from 14/118 to 45/118, $|Kmx|$ increases from 0.93 to 0.98), resulting in an unequal distribution of metal droplets along the x-direction. The increase in Q_T produces a large number of droplet dispersed phases and, to a certain extent, corresponds to a decrease in S/M, where $|K_{mx}|$ decreases, and this trend slows down with the increase in Q_B, which is caused by the interaction between top and bottom blowing. The effect of H and Q_T on $|K_{my}|$ is essentially the same as that of $|K_{mx}|$. It should be explained that with the increase in Q_T, the vertical velocity of the metal droplet detachment point and the slag phase flow velocity increase simultaneously, and the increase in the vertical velocity of the metal droplet detachment point may be larger than the increase in the slag phase flow velocity, so the increase in Q_T instead makes the y-direction distribution show non-uniformity, but this non-uniformity is the non-uniformity in the high emulsion state. As Q_B accelerates the slag layer flow, $|K_{my}|$ decreases as Q_B increases. The Q_B exceeds a certain value (≥ 0.8 Nm^3/h), which will prevent the steel droplets from moving in the y-direction, and $|K_{my}|$ increases instead.

Figure 8a,b show the relationship between the distributions of $|K_{sx}|$ and $|K_{sy}|$ in the horizontal and vertical coordinates of the dispersed phase of the slag droplet and the boundary conditions. As can be seen in the figure, the distribution of droplets in both horizontal and vertical coordinates is the same; with the increase in H (80 mm to 170 mm) and S/M (14/115 to 45/118) (when $|Ksx|$ decreases from 0.85 to 0.60, $|Ksy|$ decreases from 1.05 to 0.75), the stirring of the liquid bath decreases and the generation rate of the dispersed phase of droplets and the velocity of the flow field decreases. The decrease in the velocity of the flow field is the main influencing factor at this time. With the increase in Q_B, the stirring of the liquid bath becomes stronger, the velocity of slag droplet generation and the velocity of the flow field increase, and the increase in the flow velocity is the main influencing factor.
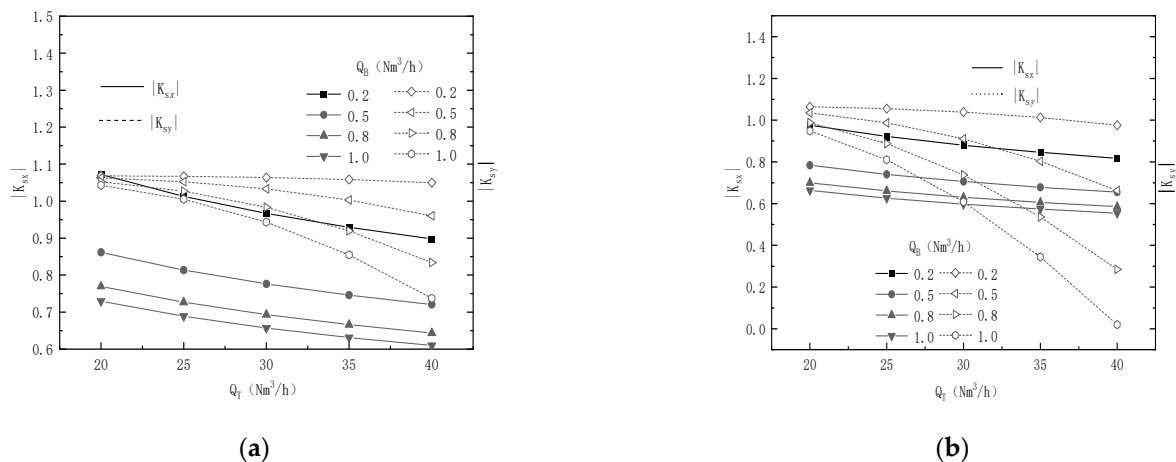

(a)   **(b)**

Figure 8. Relationship between $|K_s|$ and top blowing under various lance positions with different S/M ratios: (**a**) S/M = 45/118, H = 170 mm; (**b**) S/M = 14/118, H = 80 mm.

Under combined blowing conditions, the horizontal and vertical coordinates of the dispersed phase (slag droplets) tend to be distributed in a similar way. In a scenario with specified top and bottom blowing flow rates, an increase in the lance height or slag/metal ratio weakens the stirring of the melt pool, thus significantly lowering the generation rate of the slag droplets and the velocity of the dispersed phase. However, the decrease in liquid velocity is the determining factor behind an increase in the lance height or slag/metal ratio, thus resulting in an uneven distribution of the dispersed phase. When the lance height and slag/metal ratio are relatively fixed, with the increase in the stirring gas flow rate, especially the bottom blowing flow rate, the stirring of the metal pool becomes stronger, and the generation rate of slag droplets and the velocity of the dispersed phase are increased

drastically. The increase in the latter is greater than in the former. Therefore, the coordinate distribution of the dispersed phase becomes uniform.

4. Conclusions

(1) There is a proportional relationship between the frequency of dispersed phases and their size for each size class in the combined blowing process. The empirical relationship between the size distribution of the metal and slag dispersed phases and their scales $|M_{mf}|$, $|M_{sf}|$ and the experimental boundary conditions can be written as followss:

$$|M_{mf}| = 1.6487 \, Q_{O2}^{(-3.2043 \times 10^{-8}Q2_{N2}+8 \times 10^{-5}Q_{N2}+0.2542)} / [(S/M)^{0.0524} \, H_f^{0.3443}]$$

$$|M_{sf}| = 0.2431 tg\{0.2021Q_{O2}^{(1.2 \times 10^{-4} \, Q_{N2}+0.3158)} / [(S/M)^{0.08392}H_f^{0.139}] - 2.3815\} + 1.9551$$

(2) The size distribution of the metal drops shows extreme values with increasing top and bottom blowing intensity, and the trend becomes more pronounced with a smaller metal/slag ratio.

(3) The empirical relationships between the distribution of the metal and slag dispersed phases in the horizontal and vertical coordinates and the boundary conditions under combined blowing conditions are as follows:

$$|K_{mx}| = 0.8508(S/M)^{0.0229}H_f^{0.01004}Q_{O2}^{0.01482}(2.3378 \times 10^{-8}Q_{N2}^2 - 3.4434 \times 10^{-5}Q_{N2} + 0.9665)$$
$$|K_{my}| = 1.5938(S/M)^{0.02975}H_f^{-0.09002}Q_{O2}^{0.01963}(1.8081 \times 10^{-6}Q_{N2}^2 - 1.45 \times 10^{-3}Q_{N2} + 1.3946)$$
$$|K_{sx}| = 15.09\{1 - \exp[-10.8311(S/M)^{0.0133}H_f^{0.108}Q_{O2}^{-0.2647}Q_{N2}^{-0.2468}]\}$$
$$|K_{sy}| = 1.069\{1 - \exp[6.4407(1 - 35.1172(S/M))^{0.00828}H_f^{0.2048}Q_{O2}^{-0.4167}Q_{N2}^{-0.1974}]\}$$

the boundary conditions

$$1300 \leq H_f \leq 1900 \, mm, \, 4300 \leq Q_{O2} \leq 8600 \, Nm^3/h, \, 46 \leq Q_{N2} \leq 230 \, Nm^3/h, \, 0.1186 \leq S/M \leq 0.3814$$

(4) An increase in the bottom blowing flow rate facilitates the homogeneous distribution of the coordinates of the slag droplets, while an excessive increase is detrimental to the homogeneous distribution.

Nomenclature

Symbol	Definition
Fr_m Fr'_m	*Froude* number for the model and the prototype.
ρ_a	The density of air at 20 °C (kg/m^3).
ρ_{O2}	The density of oxygen under normal conditions (kg/m^3).
ρ_w	The density of water (kg/m^3).
ρ_m	The density of liquid steel (kg/m^3).
ρ_s	The density of slag (kg/m^3).
ρ_{N2}	The density of nitrogen gas under normal conditions(kg/m^3).
d_M d_I	Diameters for the model and the prototype (mm).
V_M V_I	The nominal velocities of the gas at the lance outlet of the model and the prototype (m/s).
e	Number of the nozzles.
Q_a Q_{O2}	The gas supply rate of the model and the prototype (Nm^3/h).
n_1, n_2	The number of bottom blowing gas nozzles of the model and the prototype (Nm^3/h).
Q_a Q_{N2}	The nominal nozzle velocities of the model and the prototype (m/s).
$d_m{}'$, $d_I{}'$	The diameters of the nozzles in the bottom lance for the model and the prototype (mm).
d_T	The droplet critical diameter (mm).
L	The range percent of dimensionless transverse coordinates of the dispersed phase.
F	The range of the coordinate distribution of the dispersed phase.
g	Gravitational acceleration (m/s^2).
h, H, H_f	The depth of molten bath, lance position of model, and actual converter (mm).
$|K_{mx}|$, $|K_{my}|$, $|K_{sx}|$, $|K_{sy}|$	The dimensionless ratio of the horizontal and vertical coordinates for the metal and slag droplets.
$|M_m|$, $|M_s|$	The size distribution of the metal and slag dispersed phases.
n, N	The number of clusters with a size equal to s, the number of clusters with a size greater than or equal to s.
DL_r	The percentage of dispersed phases in a given range to the total dispersed phases.
P	The percentage of the dimensionless coordinates of dispersed phase greater than or equal to a certain range.
Q_T, Q_{O2}, Q_B, Q_{N2}	The flow rate of top and bottom blow (Nm^3/h).
r, R, δ	The impact pit radius is represented by r; the model radius is represented by R, and δ is the slag layer thickness (mm).
s	The size of dispersed phase (pixel).
S/M	The slag/metal ratio.
u_i, $u_{i,crit}$	The interfacial flow velocity, the critical flow velocity (m/s).
x'_m, y'_m, x'_s, y'_s	The dimensionless horizontal and vertical coordinates of the metal and slag droplet.
α	The angle between escape velocity and the vertical direction.
σ	Interfacial tension (kg/s^2).

References

1. Chen, R.; Huang, Y.; Li, L.L.; Luo, Z.G. Water Modeling Study on Dispersed Phase Size Distribution and Interface Areas in Metallurgical Multiphase Reactor. *Adv. Mater. Res.* **2014**, *1052*, 567–573. [CrossRef]
2. Chen, R.; Zou, Z.S. Textural fractal dimension of slag-metal boundary in top-blowing converter with water modeling. *Chin. J. Process Eng.* **2005**, *5*, 103–106.
3. Chen, R.; Li, M.; Zou, Z.S. Fractal study on slag-metal distribution in top-blown converter using water model. *J. Iron Steel Res.* **2005**, *17*, 22–25.
4. Kaye, B.H. *A Random Walk through Fractal Dimensions*; Northeastern University Press: Shenyang, China, 1994; pp. 116–120.
5. Shen, B.M.; Shang, Z.W. *Fractal Dimension*; Seismological Press: Beijing, China, 1989; pp. 52–65.
6. Dong, L.K. *Fractal Theory and Its Applications*; Liaoning Science and Technology Press: Shenyang, China, 1991; pp. 70–82.

7. Lin, H.Y.; Li, Y.X. *Fractal Theory*; Beijing Institute of Technology Press: Beijing, China, 1992; pp. 30–34.
8. Nakanishi, K.; Kato, Y.; Nozaki, T.; Emi, T. Cold model study on the mixing rate of slag and metalBath in Q-BOP. *Tetsu Hagane* **1980**, *66*, 1307–1308. [CrossRef] [PubMed]
9. Zheng, P.R. *Steelmaking*; Metallurgical Industry Press: Beijing, China, 1994; pp. 33–41.
10. Gao, R.H.; Liu, S.H.; Zhao, Y. High-precision laser spot center positioning method for weak light conditions. *Appl. Opt.* **2020**, *59*, 1763–1768. [CrossRef] [PubMed]
11. Zhu, J.; Xu, Z.J.; Fu, D.L.; Hu, C. Laser spot center detection and comparison test. *Photonic Sens.* **2019**, *9*, 49–52. [CrossRef]
12. Huang, K.; Dai, J.; Chen, X.; Deng, W.T.; Huang, Z.J. Laser spot center detection for laser synthesizer. *Laser Infrared* **2017**, *47*, 1499–1504.
13. He, W.; Ren, M.J.; Xiao, Y. Calculation method of fly ash permeability based on image recognition. *J. Hunan Univ.* **2020**, *47*, 144–148.
14. Chen, J.Y.; Zhao, H.; Zhao, M.H. Image Processing and Multi-fractal Characteristics of Fly Ash Particles. *J. Hunan Univ.* **2021**, *48*, 205–214.
15. Nie, Z.H.; Liao, J.Y.; Zhou, S.H.; Li, B.X.; An, A.J. Image Processing and Shape Quantitative Analysis of Volcanic Cinder Particles. *J. Hunan Univ.* **2020**, *47*, 131–139.
16. Yang, S.Y.; Zhao, R.D.; Jin, H.S.; Li, F.H. Analsis on Mechanical Properties and Fractal Characteristics of Micropore Structure of Geopolymer Mortar. *J. South China Univ. Technol.* **2020**, *48*, 126–135.
17. Liu, P.; Huang, Y.P. Semi-Supervized Crack-Detection Method Based on Image-Semantic Segmentation. *Laser Optoelectron. Progress* **2021**, *58*, 317–328.
18. Zhao, L.D.; Sheng, Z.H. Applications of Fractal Models in Simulating Natural Scene. *J. Southeast Univ.* **1996**, *26*, 145–148.
19. Huang, Z.L. Fractal nature of turbulence. *Adv. Mech.* **2000**, *4*, 581–596.
20. Falconer, K.J. *Fractal Geometry-Mathematical Foundations and Applications*; Northeastern University Press: Shenyang, China, 1991; pp. 57–75.
21. Li, J.; Zhu, J.Z.; Zhu, Q.K. Review on methods of calculating fractal dimension. *J. Beijing For. Univ.* **2002**, *24*, 71–78.
22. Liu, S.J.; Li, T.R.; Liu, J.; Xie, P. Research on multi-fractals of weighted hypernetworks. *J. Univ. Sci. Technol. China* **2020**, *50*, 85–97.
23. Liu, S.J.; Li, T.R.; Liu, X.W. Network dimension: A new measure for complex networks. *Comput. Sci.* **2019**, *46*, 51–56.
24. Balka, R.; Buczolich, Z.; Elekes, M. A new fractal dimension: The topological Hausdorff dimension. *Adv. Math.* **2015**, *274*, 881–927. [CrossRef]
25. Oeters, F. *Metallurgy of Steelmaking*; Metallurgical Industry Press: Beijing, China, 1997; pp. 317–319.